15th AIAA/CEAS Aeroacoustics Conference (30th AIAA Aeroacoustics Conference)
11 - 13 May 2009, Miami, Florida

AIAA 2009-3392

Porous Airfoils: Noise Reduction and Boundary Layer Effects

Thomas Geyer* Ennes Sarradj † Christoph Fritzsche*

Aeroacoustics Group, Brandenburg University of Technology, 03046 Cottbus, Germany

The present paper describes acoustic and hot–wire measurements that were done in the aeroacoustic wind tunnel at the Brandenburg Technical University of Cottbus on various SD7003–type airfoils made of different porous (flow permeable) materials. The objective of the research is the analysis of the turbulent boundary layer properties of porous airfoils and, subsequently, of the noise generated at the trailing edge. The influence of the porous materials, characterized by their air flow resistivity, is discussed. The acoustic measurements were performed using a planar 56–channel microphone array and the boundary layer properties were measured using constant temperature anemometry. The recorded acoustic data underwent further processing by application of an advanced beamforming algorithm. A noticeable reduction of the emitted trailing edge noise was measured for the porous airfoils over a large range of frequencies. At high frequencies, some of the porous airfoils were found to generate more noise than the reference airfoil which might be due to the surface roughness noise contribution. It is found that the turbulent boundary layer thickness and the boundary layer displacement thickness of the airfoils increase with decreasing flow resistivities for both suction and pressure side. Both boundary layer thickness and displacement thickness of the non–porous airfoil are below those of the porous airfoils.

Nomenclature

c	speed of sound, m/s
c_l	chord length, m
D	directivity function
f	frequency, Hz
h	span width wetted by the flow, m
Ma	mean flow Mach number
n	scaling exponent
$OSPL$	overall sound pressure level, dB
$\langle p^2 \rangle$	far field mean square sound pressure, Pa
r	air flow resistivity, Pa s/m^2
R	distance, m
Re	chord based Reynolds number
SPL	sound pressure level, dB
Sr	chord based Strouhal number
Tu	turbulence intensity, %
u'	turbulent velocity fluctuations, m/s
$\overline{u}$	mean flow velocity, m/s
U	mean flow speed outside the boundary layer, m/s
x, y, z	cartesian coordinates
α	(geometric) angle of attack, °
δ	(99 %) boundary layer thickness, m
δ_1	boundary layer displacement thickness, m

*Research Assistant, Institute of Traffic Research, BTU Cottbus, Siemens-Halske-Ring 14, 03046 Cottbus, Germany.
†Junior Professor, Institute of Traffic Research, BTU Cottbus.

δ_2	boundary layer momentum thickness, m
δ_3	boundary layer energy thickness, m
Δp	pressure difference, Pa
Δx	sample thickness, m
ℓ	characteristic turbulence correlation scale, m
ρ	medium density, kg/m^3

Subscript

i	Variable number

I. Introduction

Against the background of rising needs for quiet aircraft, turbine blades and fans, different methods and approaches for airfoil self noise control are used and constantly improved in the field of aeroacoustics. One possible solution is the use of porous, flow–permeable materials.

Porous or partly porous airfoils as a means of noise reduction have been subject to several studies before. This includes research on the aeroacoustic and the aerodynamic effects of porous airfoils in a fluid flow. Chanaud et al.[1,2] describe the effect of porous blades on the reduction of fan noise. Savu[3] did numerical analysis on the use of porous materials to affect the pressure jump on airfoils in transsonic flow. Mineck and Hartwich[4] did extensive aerodynamic experiments with partly porous airfoils in an open jet wind tunnel. The publications by Tinetti et al.[5,6] contain the use of a passive porosity to reduce wake–stator–interaction noise. Garcia-Sagrado et al.[7] invested the trailing edge noise generation on model airfoils with different trailing edge thicknesses by measuring both surface pressure fluctuations and turbulent boundary layer velocity. Sarradj and Geyer[8] did preliminary aeroacoustic and aerodynamic measurements on porous airfoils on a set of porous airfoils. Herr[9] did research on the influence of a flow–permeable trailing edge on the noise generation. Her results also confirmed the noise reduction potential of flow permeable trailing edges.

The results described in reference[8] encourage further measurements to help understand the influence of the porous material parameters on the sound reduction and the aerodynamic performance of the porous airfoils.

The aim of the present paper is the investigation of the development of the turbulent boundary layer at porous airfoils, which are characterized by their flow resistivity, and on the subsequent generation of airfoil self noise. To this purpose, different airfoil models made completely out of porous materials were subject to a virtually non–turbulent air flow. Aeroacoustic and hot–wire measurements were then carried out in order to gain knowledge on the boundary layer properties, especially the displacement thickness, and their correlation to the airfoil self noise emission. The focus of the present research is on the turbulent boundary layer - trailing edge noise only as the most important airfoil noise source for a virtually non–turbulent inflow. According to Blake,[10] leading and trailing edge of an airfoil in a fluid flow can be viewed as independent noise sources, if

$$f > \frac{c}{c_l}, \tag{1}$$

f being the frequency, c the speed of sound and c_l the airfoil chord length. In the present research, Equation 1 leads to a lower frequency limit of approximately 1.5 kHz. Above this frequency, the trailing edge noise can therefore be examined separately.

The influence of certain boundary layer properties, especially the boundary layer displacement thickness δ_1, on the sound generation at the trailing edge has been subject to many scientific studies before, most of which are based on the work of Lighthill.[11] One fundamental study based on Lighthill's findings is the work of Ffowcs Williams and Hall.[12] They gave a formulation for the far field mean square sound pressure $\langle p^2 \rangle$ produced by a turbulent flow over a scattering halfplane:

$$\langle p^2 \rangle \propto \rho^2 \overline{u}^2 \frac{U^3}{c} \left(\frac{h\ell}{R^2} \right) \cdot \overline{D}, \tag{2}$$

with ρ being the medium density, $\overline{u}^2$ the mean–square turbulence velocity, U the mean flow speed ouside the boundary layer, h the spanwise extent wetted by the flow, ℓ a characteristic turbulence correlation scale, R the distance of the observer and $\overline{D}$ a directivity factor ($\overline{D} = 1$ for observers normal to the surface

of the plate). This analytical edge–scatter formulation describes the sound emission based on boundary layer parameters. As reported by Brooks and Marcolini[13] the usual assumptions are that the characteristic turbulence correlation scale is proportional to the turbulent boundary layer thickness δ or the turbulent boundary layer displacement thickness ($\ell \propto \delta \propto \delta_1$) and the mean turbulence velocity is proportional to the mean flow speed ($\overline{u} \propto U$). According to Equation 2 the far field sound pressure increases for an increasing characteristic turbulence correlation scale at a constant flow speed, thus for an increasing boundary layer thickness or displacement thickness. Beside this analytical model, Ffowcs Williams and Hall formulated a scaling approach for trailing edge noise that is commonly used in the field of aeroacoustics: The sound pressure level (SPL) of the sound emitted at the edge of a halfplane caused by a turbulent flow over the edge scales with a power of the flow speed U:

$$SPL_{scaled} = SPL - 10 \cdot log_{10} \left(\frac{U}{1 \text{ m/s}} \right)^n \text{ dB}, \tag{3}$$

Ffowcs Williams and Hall found the exponent to be $n = 5$. Howe[14] stated in his review of different trailing edge noise theories that the turbulent boundary layer - trailing edge noise sound power scales with the 4.6th power of the flow speed, thus leading to $n = 4.6$ in Equation 3. Additionally, Howe formulated a basic theory on the influence of the displacement thickness on the noise generated at a sharp trailing edge.[15]

Other studies concerning airfoil self noise include the work of Brooks and Hodgson,[16] who determined the influence of the trailing edge geometry, mainly the trailing edge bluntness, on the airfoil self noise. Another fundamental work is the report by Brooks, Pope and Marcolini,[17] containing detailed examinations of five main airfoil self noise sources. Their semi–empirical noise prediction model (the BPM–model), that includes a normalization based of the theory of Ffowcs Williams and Hall (see reference[13]), is still used in aeroacoustic studies today. The sound pressure is also scaled using Equation 3, the exponent ranging from approximately 4.6 to 5.0 depending on the Reynolds number. Other studies on the generation of sound at the trailing edge are the research done by Grosveld[18] and by Lowson,[19,20] both resulting in relatively simple noise prediction models for wind turbines, and the experimental work reported by Oerlemans et al.[21,22] The latter found the exponent $n = 4.5$ for the scaling of the trailing edge noise using Equation 3. A freely available software for the prediction of airfoil self noise, called NAFNoise[23] (National Renewable Energy Laboratory AirFoil Noise), exists which combines different models, for example the BPM–model mentioned above.

Additional research was done in the past to identify the influence of a certain surface roughness of a wall on the sound generation, for example by Howe,[24,25] Liu et al.[26,27] and Grissom.[28] Howe described the sound that is generated by a turbulent boundary layer flow over a rough surface, which is modeled as a distribution of rigid, hemispherical bosses on a rigid plane. He found that, in accordance to experimental data by Hersh,[29] for a given surface roughness the associated roughness noise decreases for increasing thicknesses of the turbulent boundary layer. According to his studies, roughness noise scales with the 6th power of the flow speed for small Mach numbers. The influence of a surface roughness on the boundary layer turbulence was not taken into account.

In 2006 a first study by Liu et al.[26] included an empirical and numerical model for turbulent boundary layer flow over a rough wall. The numerical model was used to predict the roughness noise from an aircraft wing and the results were compared to the trailing edge noise of a (smooth) wing of the same size and shape. They found that the roughness noise is noticeable at high frequencies, where it can be more significant than the corresponding trailing edge noise. At low frequencies on the other hand, the influence of the roughness noise on the trailing edge noise is negligible. However, the contribution of the roughness noise is proportional to the size and the density of the roughness elements. To validate the models Liu et al. did microphone array measurements on rough and smooth plates in an open jet wind tunnel, where the roughness noise of the rough plates exceeded that of the smooth plate for frequencies between approximately 1 and 2.5 kHz.

In 2007, Liu et al.[27] performed extensive microphone array experiments with one low–frequency and one high–frequency array on rough plates and compared the results to those of smooth plates. They confirmed the results from their 2006 study and found that the roughness noise of the rough plates enhanced the trailing edge noise due to an increased boundary layer thickness.

The effect of a surface roughness is widely used for the tripping of a laminar boundary layer to enforce the generation of a turbulent boundary layer (transition). The effect of tripping devices on the boundary layer transition is described in detail in references[30] and.[31]

It is, however, very difficult to describe the influence of the surface roughness in only a few parameters, because the character of the roughness of two surfaces can be quite different from each other.[32] For example,

Liu et al.[26,27] characterized the roughness of their model surfaces by a roughness height and a roughness density. In the work presented in this paper, the roughness of the different airfoils has not been measured due to the difficulties of such measurements on existing porous materials with microscopic structures that vary strongly.

II. Measurement Setup

A. Airfoil Models

One non–porous airfoil and 16 porous airfoils were used in the acoustic experiments. All airfoils have a chord length c_l of 235 mm and a span width of approximately 400 mm. The non–porous airfoil serves as a reference to enable comparisons between the different airfoils. It has a SD7003 shape,[33] which is a semi–symmetric Low–Re airfoil shape, and is tripped at both pressure and suction side at 10.6 % of the chord to ensure the existence of a turbulent boundary layer at the trailing edge (Figure 1(a)). The tripping tape has a chordwise width of 1.6 mm and a height of 0.15 mm. The trailing edge thickness is 0.5 mm. The porous airfoils had a modified SD7003 shape (Figure 1(b)), with a slightly increased trailing edge thickness of 1.59 mm. Without this modification, the trailing edges of the porous airfoils are too fragile to be produced without damage. Due to the surface roughness of the porous materials, no tripping tape needed to be applied to the porous airfoils to trigger the transition to a turbulent boundary layer.

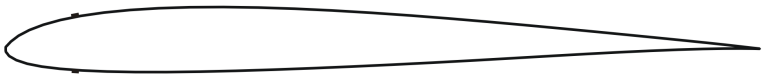

(a) Original SD7003–shaped airfoil geometry (tripping device included), used for the non–porous reference airfoil

(b) Slightly modified SD7003–shaped airfoil geometry with an increased trailing edge thickness, used for the porous airfoils

Figure 1. Comparison of the two airfoil designs, both having the same chord length c_l = 235 mm

The aim of this research is the analysis of the influence of the porous material parameters on the sound generation at the trailing edge and the turbulent boundary layer properties of the porous airfoils. Most porous materials can be be sufficiently characterized by three parameters: porosity, permeability or air flow resistivity and tortuosity. In this paper, the focus is on the air flow resistivity r only, because it is assumed to have the biggest impact on both sound and turbulent boundary layer generation.

The air flow resistivity of an open–porous material, where the inner pores are connected to each other and to the ambient fluid, is given by[34]

$$r = -\frac{\Delta p}{U \cdot \Delta x}. \tag{4}$$

Δp is the pressure drop across the porous sample with the thickness Δx and U is the percolation flow speed. That same physical issue is also governed by Darcy's Law, as for example given in reference.[35] The air flow resistivity may take values between 0 (permeable without resistance) and ∞ (impermeable).

A total of 17 airfoil models were originally used for the acoustic measurements. Only a small subset of those (given in Table 1) were also used for the hot–wire measurements. The reason for this restriction was that a great number of the 17 porous materials is soft, thus preventing the positioning of a hot–wire probe near the porous surface. Therefore, the following sections of this paper concentrate solely on the measurements and results of four rigid porous airfoil models and the non–porous reference airfoil specified in Table 1. A photograph of the porous airfoils can be seen in Figure 2.

The porous airfoils had to be assembled (in the spanwise direction) out of slices (see also Figure 2), because most of the useable porous materials are not available in an appropriate size. The slices were cut out from plates of the porous materials (between 5 mm and 50 mm thick, depending on the material) using water–cut technology. This technique was chosen in order to leave the open–porous surface intact while other techniques, like milling or laser–cutting, would have possibly destroyed or closed the pores due to the high temperatures developing during the process.

Table 1. Subset of the materials used in the acoustic measurements and in the hot–wire measurements, air flow resistivity r according to Equation 4

Number	Name	Material	flow resistivity r, Pa s/m^2	Color in figures
1	Reference	non–porous	∞	●
2	Porex	sintered PE granulate	316500	●
3	Reapor	sintered glass granulate	16500	●
4	Recemat	metal–foam	8200	●
5	M–Pore Al 45 ppi	metal–foam	1000	●

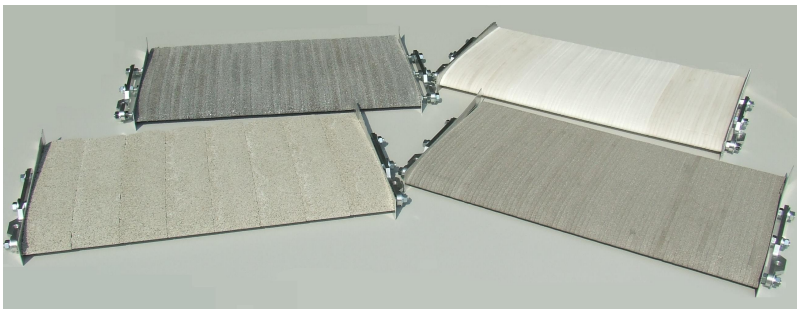

Figure 2. Photograph of the porous airfoils, from upper left to lower right: M–Pore Al 45 ppi, Porex, Reapor, Recemat)

B. Wind Tunnel

The acoustic and aerodynamic measurements were conducted in an open jet aeroacoustic wind tunnel. The circular Witoszynski–type nozzle has a diameter D of 0.2 m and a contraction ratio of 16. Note that the span width of the airfoils is greater than the diameter of the nozzle to avoid aeroacoustic and aerodynamic effects at the mountings. The turbulence intensity (in percent) of a flow is calculated using the following equation:

$$Tu = \frac{\sqrt{\overline{u'^2}}}{\overline{u}} \cdot 100\ \%, \tag{5}$$

with u' being the turbulent velocity fluctuations and $\overline{u}$ being the measured mean flow velocity. The measured turbulence intensity in a horizontal line in a distance of 1.4 mm to the nozzle exit plane is given in Figure 3(a). The measurements were done using a single wire hot–wire probe. Figure 3(a) shows that there is virtually no inflow turbulence in the core jet and the according flow velocity profiles are given in Figure 3(b), both for two flow speeds $U = 20$ m/s and $U = 50$ m/s. The wind tunnel self noise, measured for different flow speeds in a distance of 1 m from the nozzle axis, is shown in Figure 3(c). It can be seen that the overall sound pressure level (including third octave bands with center frequencies from 100 Hz to 20 kHz) is below 63 dB at a flow speed of 50 m/s.

During the acoustic measurements, the test section in front of the nozzle is surrounded by a cabin with absorbing sidewalls, providing a nearly anechoic acoustic environment at frequencies greater than approximately 500 Hz. A more detailed description of the aeroacoustic wind tunnel can be found in reference.[36]

The airfoil is mounted in the open jet and has a variable angle of attack α. It has to be noted that the results given in the present paper, especially for angles of attack that are not equal zero, can not be compared to results that would be obtained under free flow conditions. This is due to the coupling of a circular jet with a rectangular, slightly cambered airfoil and, additionally, to the fact that the airfoils have a very large dimension compared to the wind tunnel nozzle width. This results in different effects like blockage and a variation of the flow field and the loading of the airfoil in the spanwise direction. Therefore, no common methods for the correction of the angle of attack to account for the differences between free flow conditions and the open jet wind tunnel are used here, like those described by Knight and Harris[37] or Brooks et al.[38] The equations of reference[38] are basically valid for symmetric airfoils only. Nevertheless, for a lack of a more

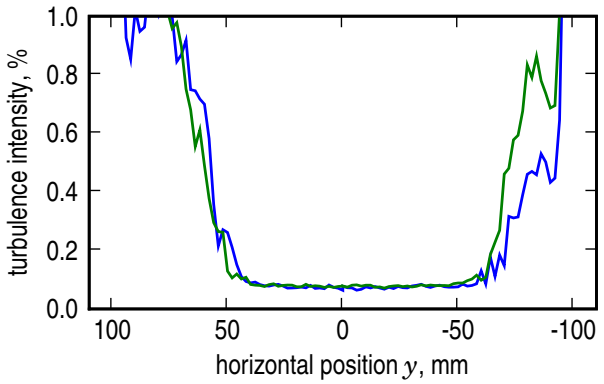

(a) Turbulence intensity Tu according to Equation 5 along a horizontal line in front of the nozzle ($U =$ 20, 50 m/s)

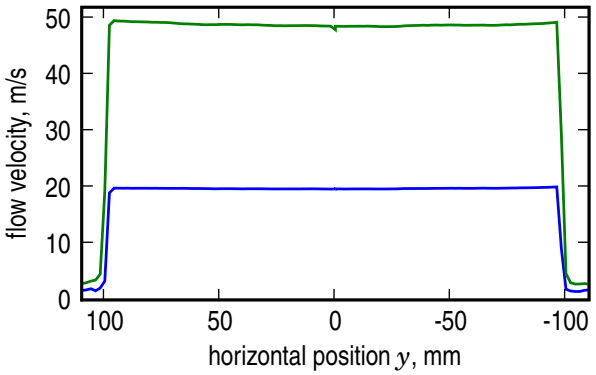

(b) Flow velocity U along a horizontal line in front of the nozzle ($U =$ 20, 50 m/s)

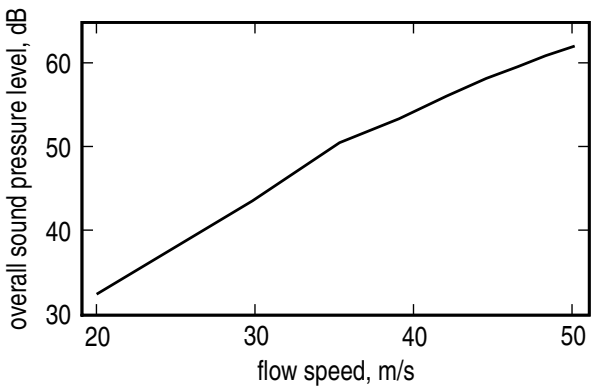

(c) Overall sound pressure level of the aeroacoustic wind tunnel at a distance of 1 m to the nozzle axis

Figure 3. Wind tunnel nozzle characteristics: Turbulence intensity Tu and flow velocity U in front of the circular nozzle (diameter 200 mm), overall sound pressure level of the wind tunnel (background noise)

suitable method, those equations are used in the present paper for the calculation of the boundary layer displacement thickness using XFOIL[39] as a means of comparison.

The following coordinate system is used for the description of both acoustic and hot–wire measurements: The x–axis is aligned with the jet axis and y- and z–axis are the horizontal (spanwise) and vertical directions, respectively, their origin being the nozzle exit plane.

C. Acoustic Measurement Setup

The acoustic measurements were carried out using a planar microphone array with 56 flush–mounted 1/4 inch microphone capsules, which was positioned 0.68 m above the airfoil model, out of the fluid flow. The aperture of the array is 1.5 m by 1.5 m. The data acquisition is achieved by a 24 bit National Instruments multichannel measurement system, further processing was done using an in-house beamforming code on a cluster of personal computers. Each measurement was conducted with a sample rate of 51.2 kHz and a total of 2048000 samples per channel, resulting in 453 MBytes of data per measurement. The effects of the refraction of sound at the shear layer of the wind tunnel on the source localization were estimated prior to the measurements according to reference.[40] The impact on the source localization are relatively small for described wind tunnel and the range of flow speeds used in the experiments. Accordingly, no correction has been used.

Figure 4 shows a schematic view of the measurement setup (view from above), including the airfoil model, the open jet wind tunnel and the 56–microphone–array.

In addition to the acoustic measurements, a six–component–balance has been used to simultaneously measure the aerodynamic performance of the different airfoils in terms of lift and drag. However, these results are not presented in this paper.

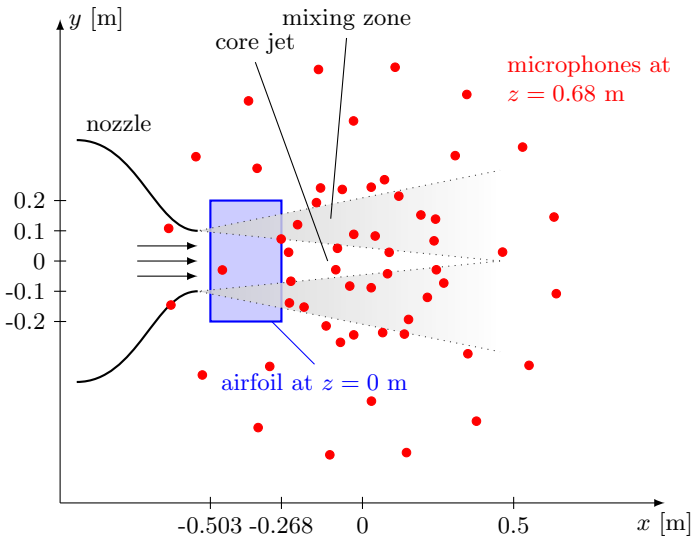

Figure 4. Schematic display of the measurement setup (top view)

D. Hot–Wire Measurement Setup

The flow velocity in the turbulent boundary layer of the airfoils was measured using Constant Temperature Anemometry (CTA). The application of a Dantec P15 type boundary layer probe (5 μm diameter, 1.25 mm long platinum-plated tungsten wire sensor) with the wire perpendicular to the streamwise velocity component enabled measurements near the surface of the airfoils. The system was calibrated after each measurement using the velocity calibration method (polynomial curve fit) using a Pitot tube. The measured voltage–time–series were transferred by the CTA measurement system in velocity–time–series by using the according calibration equation. The CTA hardware includes a low–pass filter with a cutoff–frequency of 10 kHz. The raw data were digitized using a 24–bit National Instruments data acquisition system. The sample frequency was chosen to be 25.6 kHz with a total number of 256000 samples, leading to a measurement duration of 10 s per measurement point.

The positioning of the probe was done using an ISEL lightweight traversing system with a minimum step size of 0.1 mm.

The hot–wire measurements of the velocity profiles in the vicinity of the airfoils were performed above the airfoil surface and in the wake of the airfoil. The horizontal position (y–direction) of the measurements was approximately at mid–span, inside the core jet of the wind tunnel. Eleven chordwise coordinates (x–coordinates) were chosen above the airfoil and two additional coordinates in the wake of the airfoil. Figure 5 shows the streamwise coordinates of the measurement positions. Thereby, the distance of the x–coordinates of the boundary layer measurement points from the airfoil trailing edge is 0, -5, -10, -20, -30, -45, -60, -80, -100, -120 and -140 mm (corresponding to approximately 0, 2.1, 4.3, 12.7, 19.1, 25.5, 34.0, 42.6, 51.1 and 59.6 % of the chord) towards the leading edge and the distance of the measuring points in the wake is +1 and +5 mm (0.4, 2.1 % of the chord). At least 52 measurement positions were located in the vertical (z–) direction for the measurement of the velocity profiles of the boundary layer (at every chord station on one side of the airfoil) and twice this number for the velocity measurements at the stations in the wake of the airfoil. The distance between measurement points in the vertical direction was varied: Directly above the surface, the step size was chosen to be the minimum step size of 0.1 mm, while with increasing distance from the surface the step size changed to 0.2 mm and finally to 1 mm. This led to a total of nearly 800 measurements for one flow speed U and one angle of attack. For some of the test series, this number was exceeded.

Common procedures used to determine the distance between the hot–wire and the surface of the airfoil like the Clauser plot method[41] or methods using the cooling of the wire near the surface of a (nonporous) airfoil were of no use in the described experiments. One reason is that, contrary to the theoretical flow conditions assumed for non–porous airfoils (the *law of the wall*[42]), no theory for the conditions at the surface of flow–permeable airfoils is available. The assumption of a flow velocity of $u(z = 0) = 0$ as a fixed

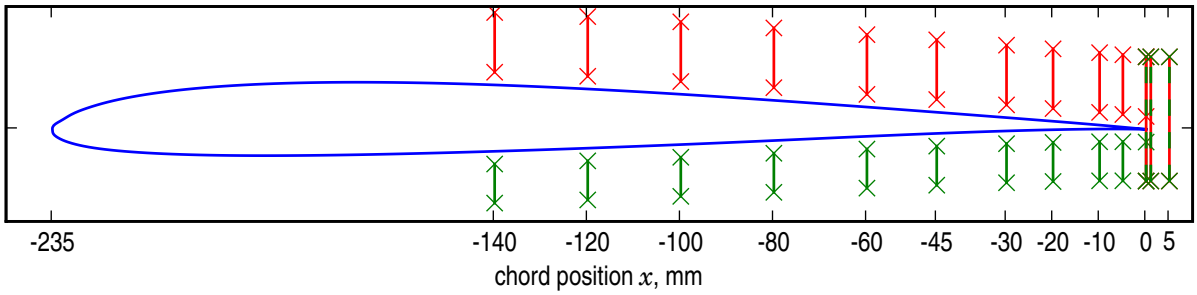

Figure 5. Positions for the CTA boundary layer measurements (eleven chordwise positions and two positions in the wake–region), given is the path in the x–z–plane along which each 52 measurements were made (red color denotes the paths on the suction side, green the paths on the pressure side of the airfoil)

boundary condition can not be made, because of a presumable flow inside the porous material. Additionally, the surface of the porous airfoils is not smooth and two of the porous airfoils are made of a metallic material and are therefore electrically conductive. Due to these reasons a more approximative and time consuming method had to be used instead for the measurements on porous airfoils: A dummy sensor with exactly the same geometry as the hot–wire probe (simply another Dantec P15 boundary layer probe without the Tungsten wire) was used to optically determine the vertical position when the prongs just touched the surface of the airfoil. Thus, the absolute accuracy of the vertical (z) position of the hot–wire probe is at the maximum equivalent to that of the traversing system (0.1 mm).

III. Data Processing

A. Acoustic Data

The raw data of the 56 microphones were further processed on a cluster of personal computers to obtain the trailing edge noise spectra. The sampled microphone signals were transformed using a Fast Fourier Transformation (FFT) with a Hanning window and 4096 samples per block. The resulting $56^2 = 3136$ cross spectra were calculated and averaged with an overlap of 50% to obtain the cross spectral matrix. The orthogonal beamforming algorithm[43] was then used to further process the acoustic data, resulting in a spatial image of the local sound pressure contributions called sound map (similar to an "acoustic photograph"). This particular algorithm was chosen after carefully testing different other beamforming algorithms, such as the CLEAN-SC beamforming method[44] and the deconvolution approach for the mapping of acoustic sources (DAMAS).[45] The orthogonal beamforming method was found to deliver the most reliable results especially for higher frequencies, where the CLEAN–SC failed to locate sound sources and the DAMAS algorithm tended to overpredict the emitted noise. Therefore, all acoustic results throughout the remaining paper were calculated using the orthogonal beamforming method. Absolute sound pressure levels were obtained by integration of the orthogonal beamfoming map over the accordant noise source region. Since this paper focusses on the generation of noise at the trailing edge and its correlation with the turbulent boundary layer, the sector chosen for the integration of the sound maps contains only the central trailing edge region of the airfoil. The airfoil leading edge and the lateral edge regions as well as the impingement region of the shear layers are not located in this sector. The resulting spectra of the power spectral density (PSD) were then transferred to third–octave–band spectra of the sound pressure level (SPL) with center frequencies between 400 Hz and 20 kHz. For some analyses, the overall sound pressure level $OSPL$ was calculated based on the resulting third–octave–band sound pressure levels. The $OSPL$ in this research is calculated as a summation of the third octave band sound pressure levels SPL_i with center frequencies between 2 kHz and 20 kHz (in agreement with Equation 1):

$$OSPL = 10 \cdot log_{10} \left(\sum_{f_m=2\text{ kHz}}^{20\text{ kHz}} 10^{[SPL_i/(10\text{ dB})]} \right) \text{dB}, \tag{6}$$

B. Hot–Wire Data

The processing of the hot–wire data was realized using self–developed code. The input data for the calculations were the digital velocity–time–series acquired by the 24–bit National Instruments system (velocity–analysis method[46]). Although a very low traversing speed of 10 mm/s was chosen, slight vibrations of the probe shortly after each step of the traversing system cannot be prevented. To counteract this effect, the first two seconds of every measured time series were omitted before the further procession of the CTA data. The remaining time domain data were then transferred to the frequency domain by using an FFT with a Hanning window and 4096 samples per block. A high–pass–filter with a cutoff–frequency of 10 Hz was used to eliminate the offset voltage and the low–frequency–turbulence contributions from the wind tunnel that are not generated at the airfoils.

To characterize the turbulent flow over the trailing edge in an incompressible flow, four different statistical flow parameters were calculated from the distribution of the mean velocity $u(z)$ (according to reference[47]):

- the boundary layer thickness δ, as the vertical distance from the airfoil surface, where the mean velocity reaches 99 % of the outer velocity,
- the boundary layer displacement thickness

$$\delta_1 = \int_{z=0}^{\infty} \left(1 - \frac{(u(z)}{U}\right)\, dz, \tag{7}$$

- the momentum thickness

$$\delta_2 = \int_{z=0}^{\infty} \left(1 - \frac{(u(z)}{U}\right) \cdot \left(\frac{(u(z)}{U}\right)\, dz \tag{8}$$

  and

- the energy thickness

$$\delta_3 = \int_{z=0}^{\infty} \left[1 - \left(\frac{(u(z)}{U}\right)^2\right] \cdot \left(\frac{(u(z)}{U}\right)\, dz. \tag{9}$$

The integration in Equation 7 through 9 was implemented using the trapezoidal rule.

IV. Results and Discussion

A. Aeroacoustic Results

The aeroacoustic measurements were conducted at 15 flow speeds ranging approximately from 26 m/s to 50 m/s. This resulted in ranges of the Mach number from approximately 0.08 to 0.15 and the chord based Reynolds number from $4{\cdot}10^5$ to $8{\cdot}10^5$. The geometric angle of attack was varied between -20° and 24° in 4°–steps.

Figure 6 shows the scaled sound pressure level for each of the five airfoils listed in Table 1 as a function of the chord based Strouhal number $Sr = \frac{f \cdot c_l}{U}$. The scaling was done using Equation 3. The scaling approach was found to give the best results for the non–porous reference airfoil when the exponent n was chosen to equal 4.6, which was subsequently used also for the porous airfoils to enable a better comparison. It can be seen from the figure that this scaling seems to be valid for the reference airfoil, because the resulting curve shows no considerable dependency on other degrees of freedom. However, this scaling approach is not valid without restrictions for the porous airfoils, although it might be a good first guess for some of them. An appropriate scaling approach that is adapted to the porous material parameters is not available yet.

Figure 7(a) shows the dependency of the overall sound pressure level of the four porous and the non–porous airfoil on the flow speed U. It reveals that the overall sound pressure level clearly depends on the flow speed U in the examined range of flow speeds. For increasing flow speeds the overall sound pressure level increases. Figure 7(b) gives the overall sound pressure level as a function of the geometric angle of attack α. It can be seen that in general the dependency of the sound generated at the airfoil trailing edge on the angle of attack is more complex than the dependency on the flow speed. For some of the airfoils (non–porous

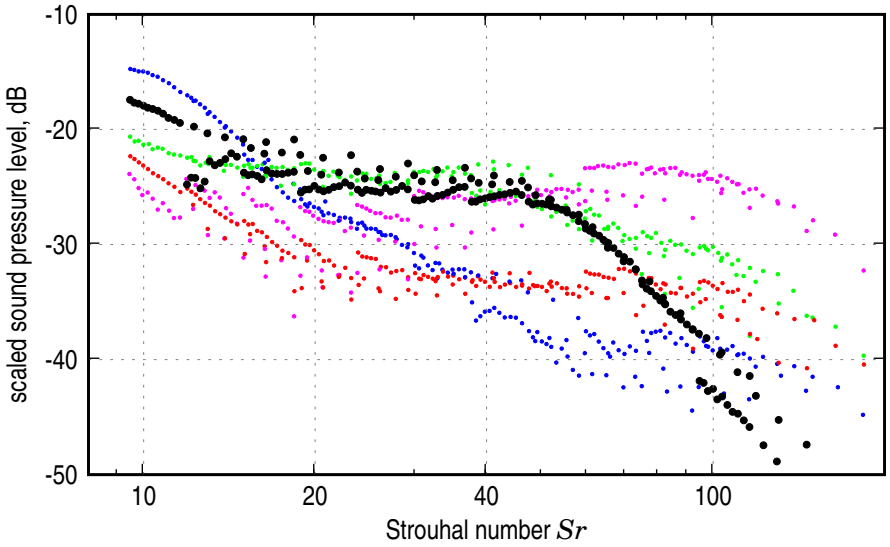

Figure 6. Overview of the sound pressure level, scaled using Eq. (3) with $n = 4.6$, as a function of the chord based Strouhal number Sr at $\alpha = 0°$, different colors denote different porous materials, bigger black dots indicate the non–porous airfoil ($r =$ — ∞, — 316500, — 16500, — 8200, — 1000 Pa s/m^2)

airfoil, $r = \infty$, and Porex, $r = 316500$ Pa s/m^2) it is rather small, at least for the range of angles examined in the present research. For the airfoil made of Recemat ($r = 8200$ Pa s/m^2) the overall sound pressure level increases when the absolute value of the geometric angle of attack increases, which is, although somewhat less distinctive, also true for the airfoils made of M–Pore Al 45 ppi ($r = 1000$ Pa s/m^2) and Reapor ($r = 16500$ Pa s/m^2).

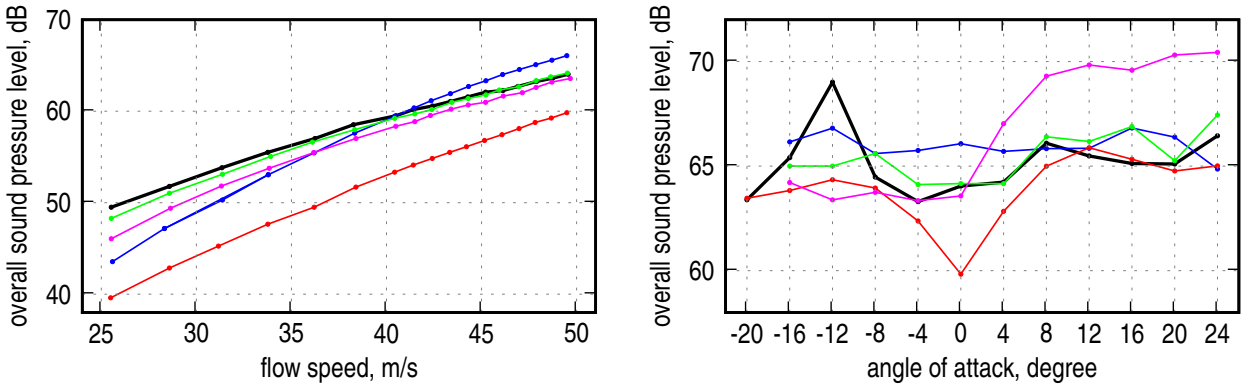

(a) Dependence on flow speed, $\alpha = 0°$

(b) Dependence on angle of attack, $U = 50$ m/s

Figure 7. Dependence of the overall sound pressure level SPL on flow speed U and (geometric) angle of attack α ($r =$ — ∞, — 316500, — 16500, — 8200, — 1000 Pa s/m^2)

Figure 8 shows the frequency dependency of the the third octave band sound pressure level generated at the trailing edge of the airfoils. The frequency step size used for the calculation was 12.5 Hz over the whole range of frequencies. It can be seen that, apart from one exception, the third octave band sound pressure level measured at the trailing edge of the porous airfoils is smaller than that of the reference airfoil (black line) over a large range of frequencies. At approximately 2.5 kHz, the spectrum of the non–porous airfoil shows a noticeable drop. The SPL measured for the airfoil made of Reapor ($r = 16500$ Pa s/m^2) exceeds the SPL of the non–porous airfoil for frequencies greater than 2.5 kHz. One possible reason might be the trailing edge of the Reapor–airfoil. The airfoil itself is made out of porous glass pellets and therefore it is very fragile. Due to some of the pellets breaking out during the assembling of the airfoil, its trailing edge

at some spanwise positions is not as even as those of the other airfoils, which might be the source of the trailing edge noise generation compared to the non–porous airfoil. For high frequencies above approximately 6 kHz, the SPL of the airfoils made of M–Pore Al 45 ppi ($r = 1000$ Pa s/m^2) exceeds the SPL of the non–porous airfoil. At low frequencies between approximately 1.5 and 3.5 kHz, the SPL of the Porex–airfoil ($r = 316500$ Pa s/m^2) is greater than that of the reference airfoil.

In general, a noticeable noise reduction can be achieved over a large range of frequencies for nearly all of the porous airfoils compared to the reference airfoil, the maximum of the noise reduction being in the order of 8 dB.

Interestingly, the influence of the increased trailing edge thickness, the *trailing edge bluntness noise*, which usually (for non–porous airfoils) results in a noticeable spectral peak, can not be distinctively recognized in Figure 8. The spectral peak due to the bluntness noise contribution of the non–porous airfoil with a trailing edge thickness of 0.5 mm can be detected from Figure 8 between approximately 10 kHz and 12 kHz. According to the BPM–model, this peak frequency shifts to lower frequencies for an increasing trailing edge thickness (for a constant chord length and unchanging airfoil shape). The bluntness noise contribution for the porous airfoils with a trailing edge thickness of 1.59 mm should therefore be visible at a frequency clearly below 10 kHz. But since no noticeable narrowband peak appears in the third octave band sound pressure level spectra of the porous airfoils, the influence of the bluntness noise contribution on the emitted trailing edge noise may be negligible.

The porosity of the examined airfoils is in each case accompanied by a certain roughness of the airfoil surface which results in a contribution of surface roughness noise to the overall trailing edge noise. But the acoustic results show that a noticeable trailing edge noise reduction is possible through the use of porous materials despite the presumable contribution of surface roughness noise. Hence, the noise reducing effect of the porosity of the airfoils seems to have a bigger impact on the overall trailing edge noise than the surface roughness. Nevertheless, the high frequency noise contribution of the porous airfoils that is visible in Figure 8 and, consequently, in Figure 6 might be originating from the surface roughness of the porous airfoils. This assumption seems to be supported by the fact that the high frequency noise emission of the porous airfoils increases for decreasing flow resistivities of the porous materials. The airfoils with the highest sound pressure levels at high frequencies are (in descending order) M–Pore Al 45 ppi ($r = 1000$ Pa s/m^2), Reapor ($r = 16500$ Pa s/m^2) and Recemat ($r = 8200$ Pa s/m^2), the materials with the lowest flow resistivities. Apparently, porous airfoils made of materials with relatively low flow resistivities (and bigger pores) would therefore exhibit a higher surface roughness than airfoils made from materials with a high flow resistivity (and small pores). In this case, further research is necessary to fully understand the influence of the surface roughness of the porous airfoils on the overall trailing edge noise emission.

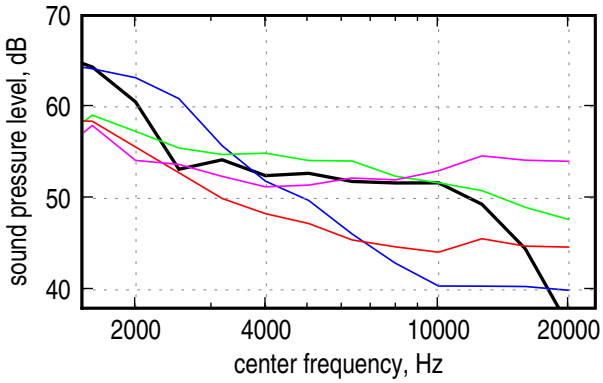

Figure 8. Resulting sound pressure level at $\alpha = 0°$ and $U = 50$ m/s ($r =$ — ∞, — 316500, — 16500, — 8200, — 1000 Pa s/m^2)

B. Boundary Layer Results

For the five airfoils from Table 1 hot–wire measurements were carried out at a mean flow speed of approximately 50 m/s and a geometric angle of attack of 0° at the positions indicated in Figure 5. For the porous airfoil made out of Recemat ($r = 8200$ Pa s/m^2) and the non–porous airfoil, further measurements were done

above the trailing edge (at $x = 0$) for varying flow speeds to capture the influence of the mean flow speed U on the generation of the turbulent boundary layer. Additional measurements were done for different angles of attack α on selected airfoils in order to understand the influence of the angle of attack on the turbulent boundary layer.

The influence of the spanwise position y on the measured boundary layer properties has been tested in preliminary experiments and was found to be negligible when inside the virtually non–turbulent core jet of the wind tunnel. Outside this core jet, the shear layer and the turbulent mixing zone of the free jet (see Figure 4) heavily affect the results of the CTA. Hence, all hot–wire measurements described in this paper were carried out inside the wind tunnel core jet with negligible deviations from the nozzle axis in the y–direction.

Figure 9 and 10 show the velocity profiles measured at the surfaces of the four porous airfoils and the reference airfoil. The upper figure in each figure presents the velocity profiles of the suction side of the airfoil, the lower figure that of the pressure side. The eleven chordwise positions and the two positions in the wake–region for each measurement series are those given in Figure 5. The two rightmost measurement positions (the two rightmost lines in each figure) were located 1 mm and 5 mm behind the trailing edge of each airfoil. The figures provide a qualitative overview of the different turbulent boundary layer thicknesses. The quantitative boundary layer properties are given in the following diagrams. However, it is clearly visible from Figure 9 that the turbulent boundary layers of the porous airfoils are thicker than that of the reference airfoil. Furthermore, the boundary layer thickness seems to increase for decreasing flow resistivities of the porous material (from Figure 9(a) to Figure 10(b)) for both suction and pressure side.

The velocity profiles measured in the wake of the airfoils are presented in Figure 11. Figure 11(a) gives the velocity profiles measured 1 mm behind the trailing edge of the airfoils. As also shown in Figure 9 and 10 it can be seen from this velocity profiles that with decreasing flow resistivities r the boundary layer thickness increases. At the pressure side ($z < 0$) the sequence of the measured boundary layer thicknesses (from lower to higher values: non–porous airfoil, Porex, Reapor, Recemat, M–Pore) is exactly consistent with the reversed order of the flow resistivities r of the according porous materials. At the suction side ($z > 0$) the boundary layer thickness of the airfoil made of Porex ($r = 316500$ Pa s/m^2) is smaller than that of the airfoil made of Reapor ($r = 16500$ Pa s/m^2), despite its higher flow resistivity. This effect has to be further analysed. Figure 11(b) then shows the velocity profiles at a position 5 mm behind the trailing edge of the airfoils. Both Figure 11(a) and 11(b) implicate that, despite a presumable flow inside the porous materials, the velocity directly at the surface of the airfoil ($z = 0$) is very small, although not necessarily equal zero. Interestingly, the porous consistency of the materials has an influence on the wake behind the trailing edge, as can be seen in Figure 11(b). This is especially visible for the airfoil made of M–Pore Al 45 ppi, the material with the lowest flow resistivity of 1000 Pa s/m^2, where a noticeable increase of the flow velocity directly behind the trailing edge was measured.

The statistical flow parameters of the turbulent boundary layers (displacement thickness, momentum thickness and energy thickness) calculated with Equation 7 through 9, are presented in Figure 12(a), 12(b) and 12(c), respectively. The boundary layer displacement thickness δ_1 of the porous airfoils is considerably greater than that of the non–porous reference airfoil (see Figure 12(a)) for both suction- and pressure side. At the airfoil with the lowest flow resistivity (M–Pore Al 45 ppi, $r = 1000$ Pa s/m^2) the greatest boundary layer displacement thickness was measured while at the two porous airfoils with the highest flow resistivities, namely Porex ($r = 316500$ Pa s/m^2) and Reapor ($r = 16500$ Pa s/m^2), the smallest displacement thicknesses of the porous airfoils have been determined. And while the displacement thicknesses for suction side and pressure side of the non–porous airfoil seem to be very similar, it differs noticeably for the porous airfoils. A possible reason for this difference might be a fluid flow through the porous airfoils. The order of the airfoils regarding their generated turbulent boundary layer displacement thickness in general seems to be similar to that found in Figure 11, 9 and 10: For decreasing flow resistivities, the displacement thickness apparently increases. This is indeed true for the displacement thickness measured at the suction side. For the boundary layer displacement thickness of the pressure side there is only one exception: The displacement thickness of the airfoil made of Reapor ($r = 16500$ Pa s/m^2) is smaller than that of the airfoil made of Porex ($r = 316500$ Pa s/m^2), despite the lower flow resistivity of the latter material. For validation purposes, the boundary layer displacement thickness of a non–porous SD7003–shaped airfoil with the same chord length of 235 mm was calculated directly at the trailing edge position on both suction and pressure side using XFOIL. The results are included in Figure 12(a). The measured displacement thicknesses of the reference airfoil are somewhat below that calculated, but this deviation between theory and measurement seems acceptable

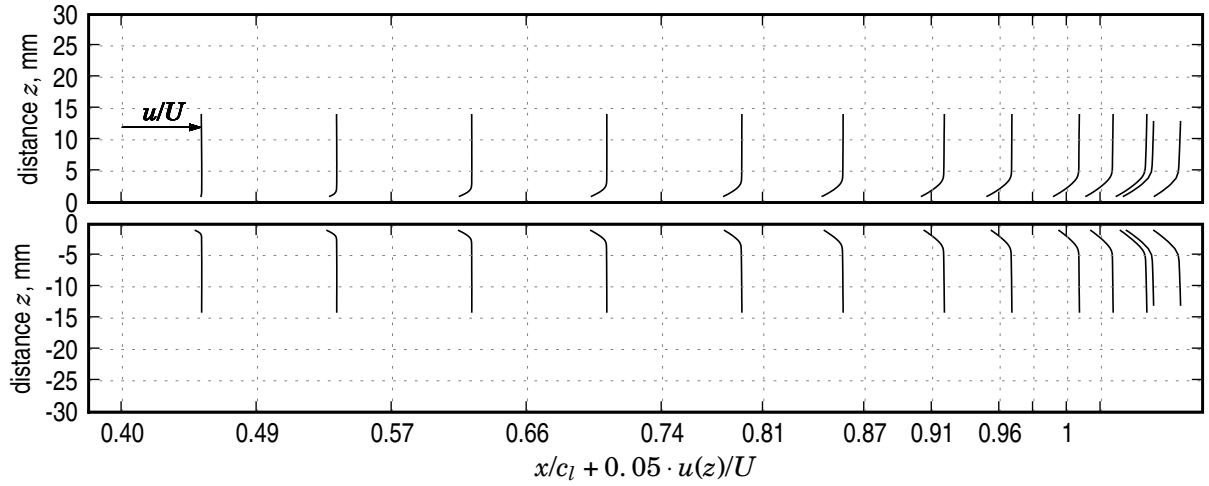

(a) Non–porous airfoil, $r = \infty$

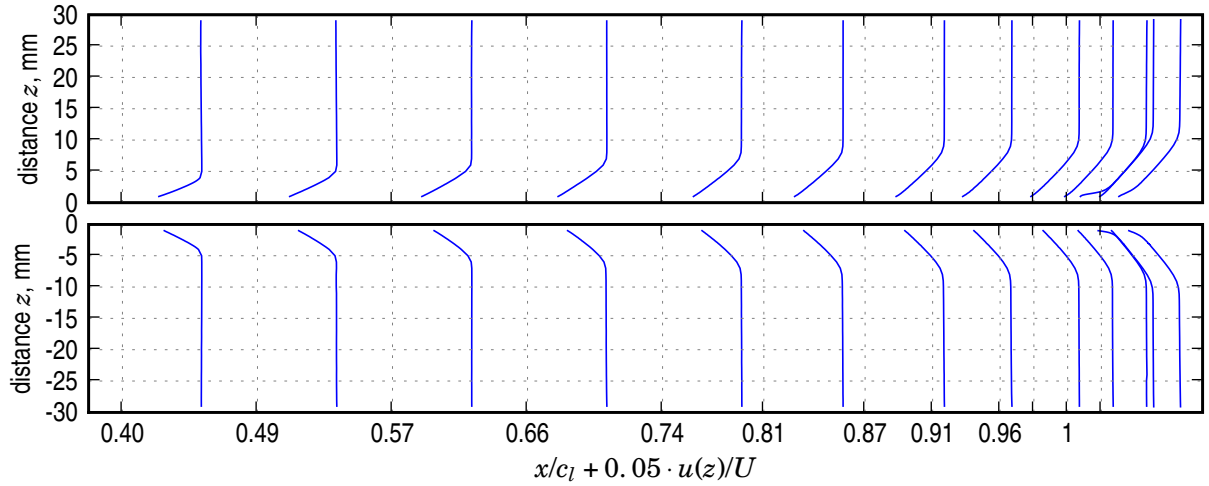

(b) Porex, $r = 316500$ Pa s/m^2

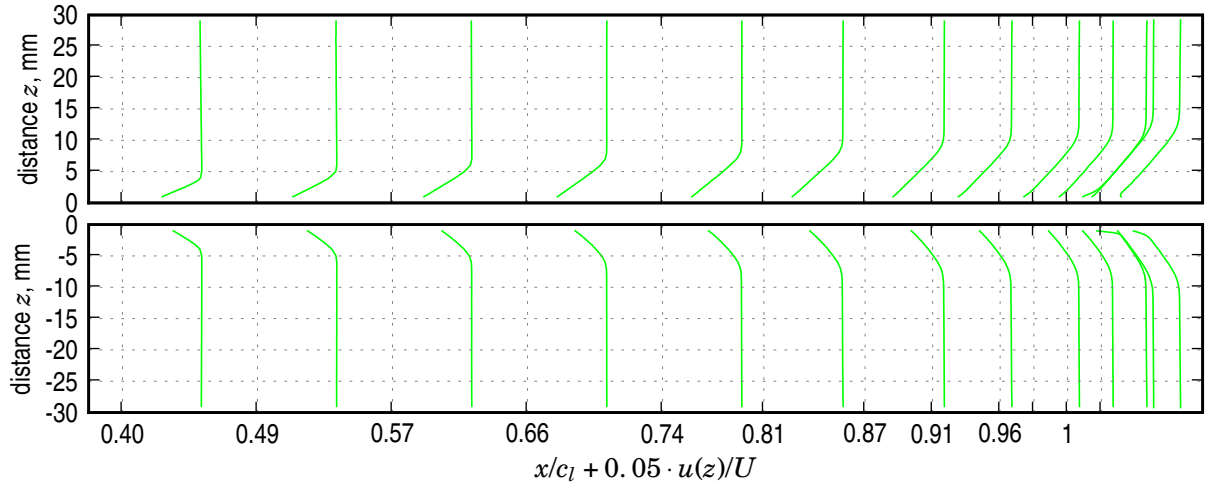

(c) Reapor, $r = 16500$ Pa s/m^2

Figure 9. Measured velocity profiles at suction- (upper figure) and pressure–side (lower figure) of the airfoils,α = 0° and U = 51 m/s (r = ∞, 316500, 16500, 8200, 1000 Pa s/m^2). Please note that the two rightmost lines in each figure were measured in the wake of the airfoil, not above its surface (see Figure 5).

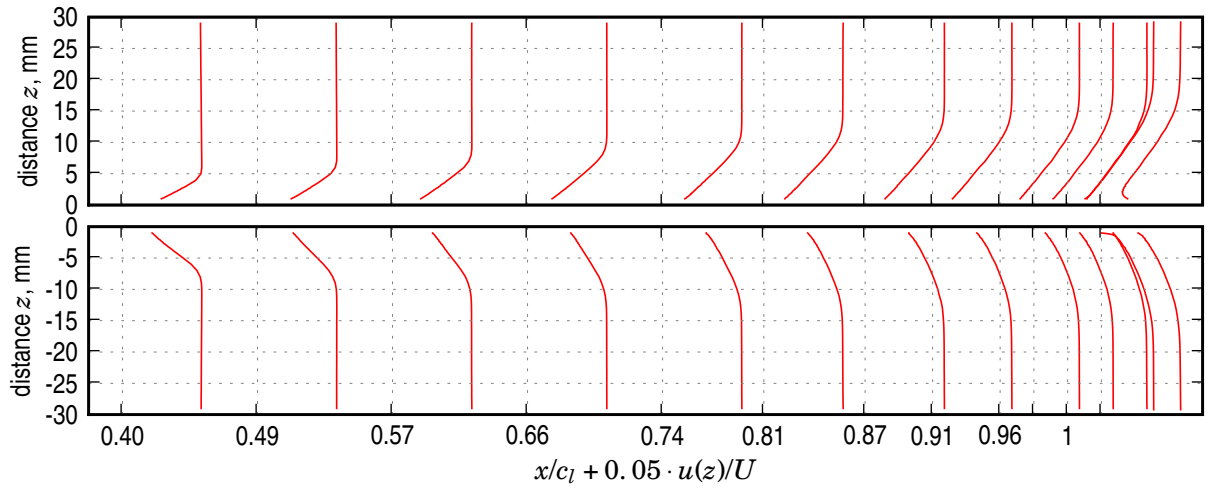

(a) Recemat, $r = 8200$ Pa s/m^2

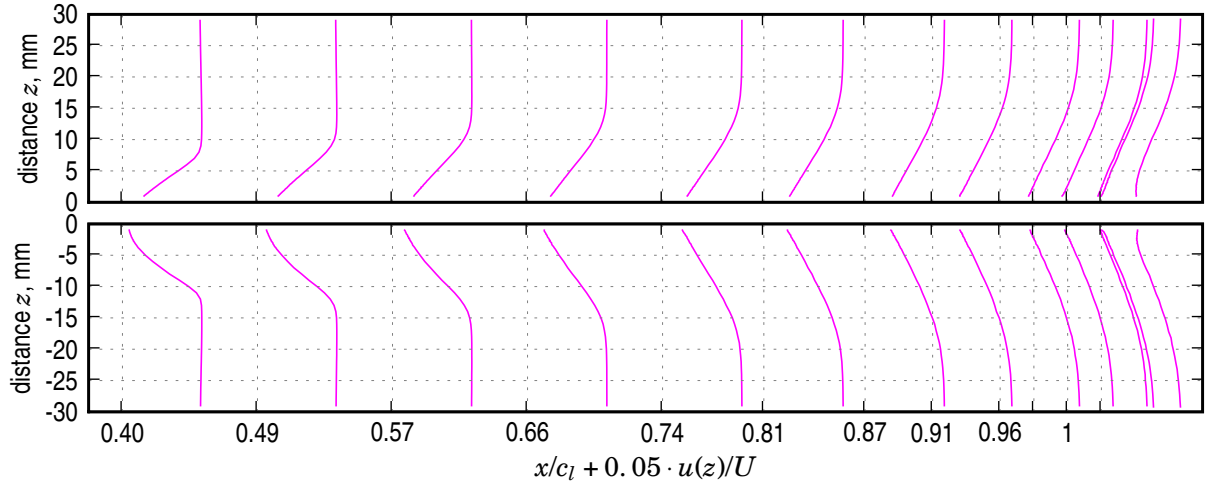

(b) MPore, $r = 1000$ Pa s/m^2

Figure 10. same as in Figure 9

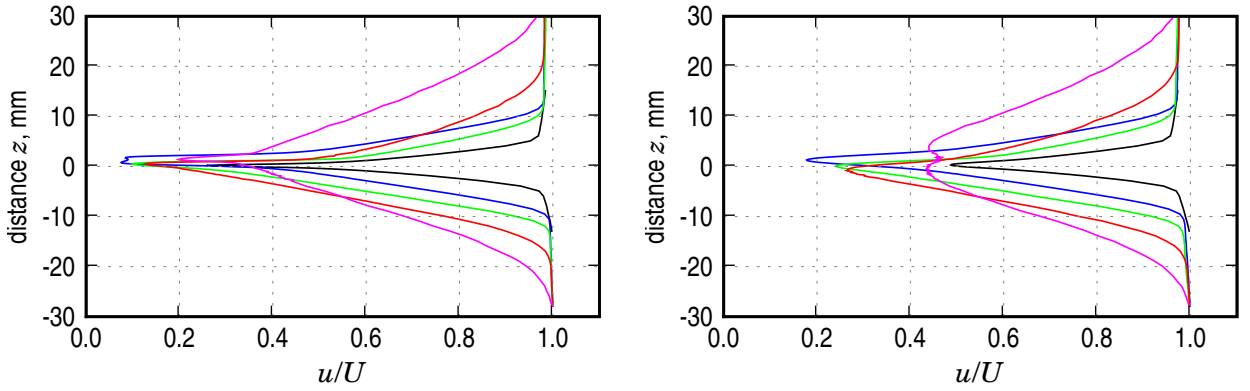

(a) Measured velocity profiles in the wake (1 mm behind the airfoil trailing edge)

(b) Measured velocity profiles in the wake (5 mm behind the airfoil trailing edge)

Figure 11. Measured velocity profiles in the wake, $\alpha = 0°$ and $U = 51$ m/s ($r =$ ∞, 316500, 16500, 8200, 1000 Pa s/m^2). Note that the given distance in the vertical direction relates to the upper side of the trailing edge.

when the more approximative procedure to determine the distance between hot–wire and airfoil surface (as described in the setup of the hot–wire measurements) is kept in mind.

The results of the calculation of the boundary layer momentum thickness, Figure 12(b), and the energy thickness, Figure 12(c), are consistent to those of the displacement thickness: With decreasing flow resistivities, the momentum thickness as well as the energy thickness decreases. This is especially true for the measurements at the suction side. At the pressure side, however, the porous material with the second highest flow resistivity (Reapor, $r = 16500$ Pa s/m^2) generates the lowest momentum thickness and energy thickness of the porous materials.

The influence of the mean flow velocity U on the boundary layer displacement thickness δ_1 is shown in Figure 13(a) for the reference airfoil and the porous airfoil made of Recemat ($r = 8200$ Pa s/m^2). Again, the boundary layer displacement thickness calculated for the non–porous airfoil using XFOIL is included in the figure. And while δ_1 slightly increases with increasing flow speed U for both measured cases, it slightly decreases for the calculation. But again, the difference between measured and calculated displacement thickness of the non–porous airfoil is acceptable due to the reasons mentioned above.

The dependence of δ_1 on the angle of attack is given in part in Figure 13(b) for three geometric angles of attack (0°, +4° and +8°) and only a subset of the porous airfoils. It is clearly visible that the angle of attack has a strong influence on the boundary layer displacement thickness of the porous airfoils, while its influence is barely visible for the reference airfoil. Again, the calculated boundary layer displacement thickness is given in the figure for both suction- and pressure side (in Figure 13(b), however, the markers denoting the XFOIL–results for the individual angles of attack are positioned almost one upon the other and therefore become indistinguishable from each other).

The results of the hot–wire measurements in relation to the acoustic results indicate that despite an increasing boundary layer displacement thickness of the porous airfoils, their overall trailing edge noise emission decreases and is noticeably below that of the reference airfoil. The turbulent boundary layer thickness as well as the boundary layer displacement thickness of the porous airfoils clearly depend on the air flow resistivity of the materials: For the examined porous materials the boundary layer thickness and the displacement thickness increase for decreasing flow resistivities. For non–porous airfoils on the other hand, the theory by Ffowcs Williams and Hall (Equation 2) gives the opposite relation between the characteristic turbulent correlation scale and the noise generated at the trailing edge: If the mean flow speed is kept constant, the far field mean square sound pressure is proportional to the characteristic turbulent correlation scale. The characteristic turbulent correlation scale is thereby assumed to be proportional to the boundary layer thickness or the displacement thickness and the mean turbulence velocity is assumed to be proportional to the mean flow speed. This assumption can clearly not be made for the porous airfoils. Due to this reason, established airfoil self noise prediction models that are based on the analysis of Ffowcs Williams and Hall with the above mentioned assumptions, like the BPM–model or the more simple model by Lowson, can not be used without general modifications for the estimation of trailing edge noise generated at porous airfoils.

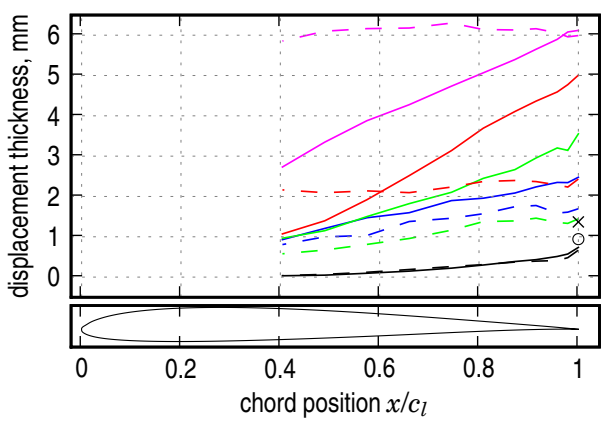

(a) Boundary layer displacement thickness, calculated using Equation 7 (The "x" and "o" denote the displacement thickness calculated using XFOIL for suction side and pressure side, respectively.)

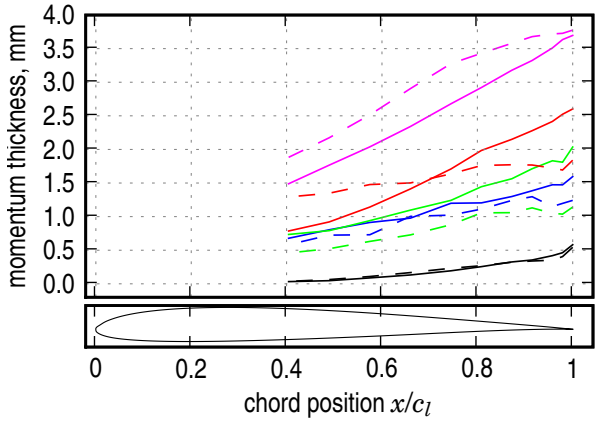

(b) Boundary layer momentum thickness, calculated using Equation 8

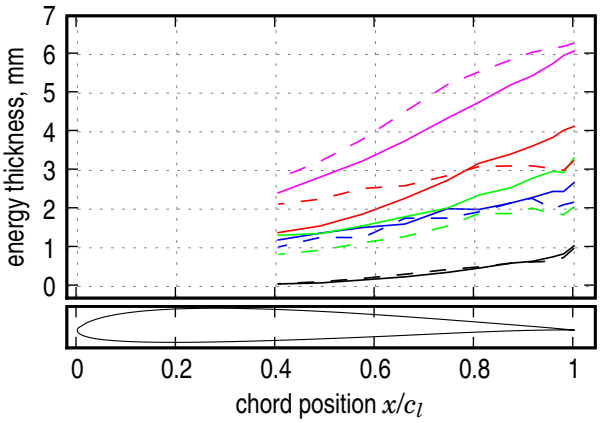

(c) Boundary layer energy thickness, calculated using Equation 9

Figure 12. Statistic flow parameters, $\alpha = 0°$ and $U = 51$ m/s, the continuous line represents the results from the suction side, the dashed line those from the pressure side of each airfoil ($r =$ — ∞, — 316500, — 16500, — 8200, — 1000 Pa s/m^2). Note that the schematic of the airfoil is given for illustrative purposes only, the distance given on the ordinate refers to the airfoil surface as origin.

The results presented in this paper may serve as a basis to develop a model for the influence of the porous material parameters on the trailing edge noise generation.

V. Conclusions

The present paper describes the research on the trailing edge noise reduction and the boundary layer properties of porous airfoils. The main objective is the investigation of the influence of the air flow resistivity of the porous materials on both the generation of noise at the trailing edge and on the turbulent boundary layer displacement thickness of the airfoils. Therefore, aeroacoustic measurements using a 56 microphone array and the orthogonal beamforming method as well as constant temperature anemometry measurements with a boundary layer probe have been performed on a set of SD7003–shaped airfoils. Four airfoils were made of flow permeable materials with different air flow resistivities and one non–porous airfoil served as a reference.

Apart from few exceptions, the sound pressure level generated at the trailing edge of the porous airfoils was lower than that of the reference airfoil over a large range of frequencies. For high frequencies above approximately 8 kHz, two of the porous airfoils produced more noise than the non–porous airfoil. This might be due to the contribution of the surface roughness noise, which is usually noticeable at high frequencies.

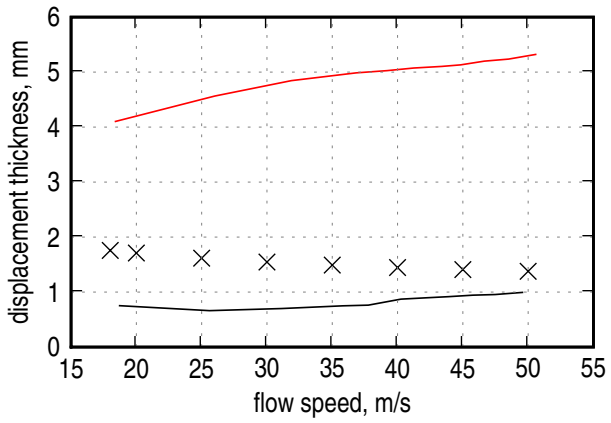

(a) Dependence of the boundary layer displacement thickness δ_1 on the mean flow velocity U (The "x" denote the displacement thickness calculated using XFOIL for the suction side)

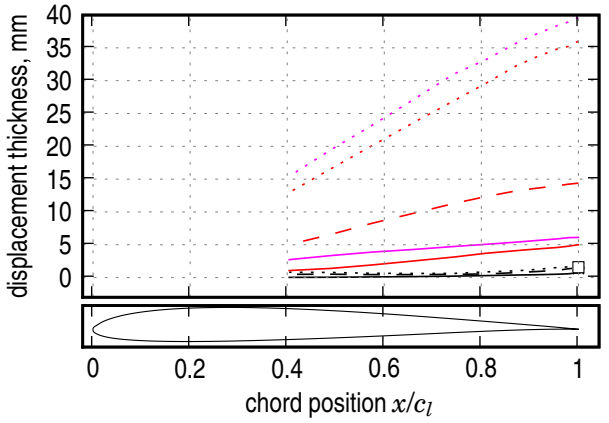

(b) Dependence of the boundary layer displacement thickness δ_1 on the angle of attack α, solid line: 0°, dashed line: +4°, dotted line: +8° (The markers denote the displacement thickness calculated using XFOIL for $\alpha = 0°$ ("x"), 4° ("o") and 8° (square marker).)

Figure 13. Dependence of the (suction side) boundary layer displacement thickness on the mean flow velocity U and the angle of attack α ($r =$ — ∞, — 8200, — 1000 Pa s/m^2). Note that the schematic of the airfoil is given for illustrative purposes of the chordwise position only, the distance given on the ordinate refers to the airfoil surface.

This means that a considerable sound reduction effect was measured for the trailing edge noise of the porous materials despite a presumed contribution of surface roughness noise. A classical scaling approach that scales the generated sound pressure level with the 4.6th power of the flow speed was tested on the airfoils. While it yields good results for the reference airfoil, it does not fit very well for the porous airfoils.

It was found that the turbulent boundary layer thickness and the boundary layer displacement thickness of the porous airfoils clearly exceed those of the non–porous airfoil for both suction and pressure side. The general trend is that the displacement thickness of the porous airfoils increases for decreasing flow resistivities.

Contrary to the theory for non–porous airfoils, an increasing turbulent boundary layer thickness and boundary layer displacement thickness result in a decreasing noise generation at the trailing edge of porous airfoils.

Acknowledgments

This research was sponsored by the *Deutsche Forschungsgemeinschaft* in the priority program 1207, "Strömungsbeeinflussung in der Natur und Technik", under the grant number SA 1502/1-2.

References

[1]R. C. Chanaud. Noise reduction in propeller fans using porous blades at free-flow conditions. *The Journal of the Acoustical Society of America*, 51:15 – 18, 1971.

[2]R. C. Chanaud, Ning Kong., and R. B. Sitterding. Experiments on porous blades as a means of reducing fan noise. *The Journal of the Acoustical Society of America*, 59:564 – 575, 1976.

[3]G. Savu and O. Trifu. Porous airfoils in transonic flow. *AIAA Journal*, 22:989 – 991, 1984.

[4]R.E. Mineck and P.M. Hartwich. Effect of full-chord porosity on aerodynamic characteristics of the naca 0012 airfoil. *NASA Technical Paper 3591*, 1996.

[5]A.F. Tinetti, J.F. Kelly, S.X.S. Bauer, and R.H. Thomas. On the use of surface porosity to reduce unsteady lift. *31st AIAA Fluid Dynamics Conference and Exhibit*, 2001.

[6]A.F. Tinetti, J.F. Kelly, R.H. Thomas, and S.X.S. Bauer. Reduction of wake-stator interaction noise using passive porosity. *40th AIAA Aerospace Sciences Meeting and Exhibit*, 2002.

[7]A. Garcia-Sagrado, T. Hynes, and H. Hodson. Experimental investigation into trailing edge noise sources. *12th AIAA/CEAS Aeroacoustics Conference*, 2006.

[8]E. Sarradj and T. Geyer. Noise generation by porous airfoils. *13th AIAA/CEAS Aeroacoustics Conference*, 28, 2007.

[9]M. Herr. A noise reduction study on flow-permeable trailing-edges. Technical report, Deutsches Zentrum für Luft- und Raumfahrt (DLR), Institute of Aerodynamics and Flow Technology, 2007.

[10]W.K. Blake. *Mechanics of Flow-Induced Sound and Vibration, Volume I: General Concepts and Elementary Sources*. Academic Press, Inc., 1986.

[11]M.J. Lighthill. On sound generated aerodynamically. *Proceedings of the Royal Society of London. Series A, Mathematical and Physical Sciences*, 211:564–587, 1952.

[12]J. E. Ffowcs Williams and L. H. Hall. Aerodynamic sound generation by turbulent flow in the vicinity of a scattering halfplane. *Journal of Fluid Mechanics*, 40:657 – 670, 1970.

[13]T.F. Brooks and M.A. Marcolini. Scaling of airfoil self-noise using measured flow parameters. *AIAA Journal*, 23:207 – 213, 1985.

[14]M. S. Howe. A review of the theory of trailing edge noise. *Journal of Sound and Vibration*, 61:437 – 465, 1978.

[15]M. S. Howe. The displacement–thickness theory of trailing edge noise. *Journal of Sound and Vibration*, 75:239 – 250, 1981.

[16]T. F. Brooks and T. H. Hodgson. Trailing edge noise prediction from measured surface pressures. *Journal of Sound and Vibration*, 78:69 – 117, 1981.

[17]T. F. Brooks, D. S. Pope, and M. A. Marcolini. Airfoil self-noise and prediction. *NASA Reference Publication 1218*, 1989.

[18]F.W. Grosveld. Prediction of broadband noise from horizontal axis wind turbines. *Journal of Propulsion*, 1:292 – 299, 1985.

[19]M.V. Lowson. Assessment and prediction of wind turbine noise. *Flow Solutions Report*, 92/19:1–59, 1992.

[20]M. V. Lowson. A new prediction model for wind turbine noise. In *Renewable Energy, 17 - 19 November 1993*, 1993.

[21]S. Oerlemans and P. Migliore. Aeroacoustic wind tunnel tests of wind turbine airfoils. *AIAA Journal*, 3042, 2004.

[22]S. Oerlemans. Wind tunnel aeroacoustic tests of six airfoils for use on small wind turbines. Technical report, National Renewable Energy Laboratory, 2004.

[23]P. Moriarty. *NAFNoise User Guide*. National Wind Technology Center, 2005.

[24]M. S. Howe. On the generation of sound by turbulent boundary layer flow over a rough wall. *Proceedings of the Royal Society of London A*, 395:247 – 263, 1984.

[25]M. S. Howe. Surface pressures and sound produces by turbulent flow over smooth and rough walls. *Journal of the Acoustical Society of America*, 90:1041 – 1047, 1991.

[26]Y. Liu, A. P. Dowling, and H.-C. Shin. Effects of surface roughness on airframe noise. *12th AIAA/CEAS Aeroacoustics Conference*, 2006.

[27]Y. Liu, A. P. Dowling, H.-C. Shin, and A. R. Quayle. Experimental study of surface roughness noise. *13th AIAA/CEAS Aeroacoustics Conference*, 2007.

[28]D. L. Grissom. *A Study of Sound generated by a Turbulent Wall Jet Flow over Rough Surfaces*. PhD thesis, Virginia Polytechnic Institue and State University, 2007.

[29]A. S. Hersh. Experimental investigation of surface roughness generated flow noise. *8th AIAA Aeroacoustics Conference Paper 83-0786*, 1983.

[30]A. L. Braslow and E. C. Knox. Simplified method for determination of critical height of distributed roughness particles for boundary-layer transition at mach numbers from 0 to 5. Technical report, National Advisory Committee for Aeronautics, Langley Aeronautical Laboratory, 1958.

[31]J. B. Barlow, W. H. Rae, and A. Pope. *Low–Speed Wind Tunnel Testing, 3rd edition*. John Wiley & Sons, New York, 1999.

[32]J.A. Schetz. *Boundary Layer Analysis*. Prentice Hall, Eaglewood Cliffs, New Jersey, 1993.

[33]M.S. Selig, J. Donovan, and D. Fraser. *Airfoils at Low Speeds*. SoarTech Aero Publications, 1989.

[34]ISO9053. Acoustics – materials for acoustical applications – determination of airflow resistance. Technical report, International Organization for Standardization, 1993.

[35]A. E. Scheidegger. *The Physics of Flow through Porous Media, 3. Edition*. University of Toronto Press, 1974.

[36]E. Sarradj, C. Fritzsche, T. Geyer, and J. Giesler. Acoustic and aerodynamic design and characterization of a small-scale aeroacoustic wind tunnel. *Applied Acoustics*, 70:1073 – 1080, 2009.

[37]M. Knight and T. A. Harris. Experimental determination of jet boundary corrections for airfoil tests in four open wind tunnel jets of different shapes. Technical report, NACA, Report No. 361, 1930.

[38]T. F. Brooks, M. A. Marcolini, and D. S. Pope. Airfoil trailing edge flow measurements and comparison with theorie incorporating open wind tunnel corrections. In *AIAA-84-2266, AIAA/NASA 9th Aeroacoustics Conference*, 1984.

[39]M. Drela. Xfoil: An analysis and design system for low reynolds number airfoils. In *Conference on Low Reynolds Number Aerodynamics, University of Notre Dame*, 1989.

[40]R.K. Amiet. Refraction of sound by a shear layer. *Journal of Sound and Vibration*, 58:467 – 482, 1978.

[41]C. Tropea, A. L. Yarin, and J. F. Foss, editors. *Springer Handbook of Experimental Fluid Mechanics*. Springer Verlag Berlin Heidelberg, 2007.

[42]P. Bradshaw and G. P. Huang. The law of the wall in turbulent flow. *Proceedings of the Royal Society of London A*, pages 165 – 188, 1995.

[43]E. Sarradj. Quantitative source spectra from acoustic array measurements. *Berlin Beamforming Conference (BeBeC)*, 2008.

[44]P. Sijtsma. Clean based on spatial source coherence. *13th AIAA/CEAS Aeroacoustics Conference*, 2007.

[45]T. F. Brooks and W. M. Humphreys. A deconvolution approach for the mapping of acoustic sources (damas) determined from phased microphone arrays. *10th AIAA/CEAS Aeroacoustics Conference*, 2004.

[46]H. H. Bruun. *Hot–Wire Anemometry*. Oxford Science Publications, 1995.

[47]H. Schlichting and K. Gersten. *Boundary Layer Theory*. Springer-Verlag Berlin, 2000.